Measured shear rates in large dry and wet snow avalanches

Martin KERN,* Perry BARTELT, Betty SOVILLA, Othmar BUSER

WSL Institute for Snow and Avalanche Research SLF, Flüelastrasse 11, CH-7260 Davos-Dorf, Switzerland
E-mail: kern@slf.ch

ABSTRACT. We present estimates of internal shear rates of real-scale avalanches that are based on velocity measurements. Optical velocity sensors installed on the instrument pylon at the Swiss Vallée de la Sionne test site are used to measure flow velocities at different flow heights of three large dry and wet snow avalanches. Possible sources of error in the correlation analysis of the time-lagged reflectivity signals measured by optical sensors are identified for real-size avalanches. These include spurious velocities due to noise and elongated peaks. An appropriate choice of the correlation length is essential for obtaining good velocity estimates. Placing restrictions on the maximum possible accelerations in the flow improves the analysis of the measured data. Coherent signals are found only in the dense flowing cores. We observe the evolution of shear rates at different depths between the front and tail of the flowing avalanche. At the front, large shear rates are found throughout the depth; at the tail, plug flows overriding highly sheared layers near the bottom of the flow are observed. The measured velocities change strongly with height above the ground and fluctuations around the measured mean velocity can be identified. We find that the dense flows are laminar, undergoing a transition from supercritical to subcritical flow behaviour from the head to the tail. Furthermore, we provide real-scale experimental evidence that the mean shear rate and the magnitude of velocity fluctuations increase with the mean discharge.

INTRODUCTION

Experimental investigation of real-scale avalanches is essential to advance and validate theories of avalanche motion (Issler, 2003). Starting with the pioneering work of Schaerer and Salway (1980) and Gubler (1987), real-scale experiments have been used to study large dry–mixed avalanches (Rammer and others, 1998; Rammer, 2004; McElwaine and Turnbull, 2005), snow-cover entrainment and mass balance (Sovilla and others, 2006), avalanche impact pressures (Schaerer and Salway, 1980; Schaer and Issler, 2001; Sovilla and others, 2008a), the effect of catching dams (Lied and others, 2002, 2004; Baillifard, 2007) and front velocities (Rammer, 2004; Rammer and others, 2007).

In this paper, we discuss the possibilities and limitations of using optical velocity sensors to capture internal velocity profiles of real-scale avalanches. The distribution of internal flow velocities is particularly important in avalanche science, since it provides insight into the constitutive relations governing the distribution of shear in the avalanche body. Measured velocity profiles and shear rates not only reflect the rheology of flowing snow, but also the interaction of the flow with the ground layer, thus providing information on the basal boundary conditions of real-scale avalanches.

Optical measurements of velocity and shear rates in flowing avalanches were pioneered by Nishimura and others (1993) and Dent and others (1998). Improvements of the initial design were made by Tiefenbacher and Kern (2004). However, until now, reliable measurements have been restricted to small-scale avalanches at the Revolving Door site, Montana, USA (Dent and others, 1998) and small-scale snow-chute experiments in Switzerland (Kern and others, 2004) and France (Bouchet and others, 2003).

Optical velocity measurements on large-scale avalanches are difficult since the behaviour of the avalanche – its speed, density, flow height and even flow direction – cannot be controlled. In such conditions, data obtained from optical sensors must be carefully scrutinized to avoid erroneous interpretation. The accuracy of optical velocity measurements, which exploit the correlation of time-lagged signals, is subject to fundamental constraints (McElwaine and Tiefenbacher, 2003). Furthermore, ambiguities in the obtained velocity data are caused by the confined spatio-temporal resolution of the measurement devices and by residual electronic noise. These sources of error are closely related to the specific sensor set-up. Eliminating them requires data processing with close regard to experimental conditions for each event.

We present optical-sensor velocity measurements of three large snow avalanches at the Swiss Vallée de la Sionne test site. Two of the avalanches were large dry snow avalanches; the third was a large wet snow avalanche. Possible sources of error encountered in the data analysis are identified and discussed. At the present stage of our understanding, it is impossible to derive general relationships governing the shearing of avalanching snow from the measurements. We attempt to demonstrate how optical velocity measurements may contribute to solving this problem.

METHODS

The Vallée de la Sionne test site

Natural and artificially released avalanches can be investigated at the real-scale test site in the Vallée de la Sionne (VdlS), canton Valais, Switzerland. The avalanche track is ~2700 m long with a vertical drop of 1300 m. A 20 m high mast is situated at the start of the run-out zone of the track. It is instrumented with measurement devices for impact pressure, flow velocity, density, flow height and air pressure (in the
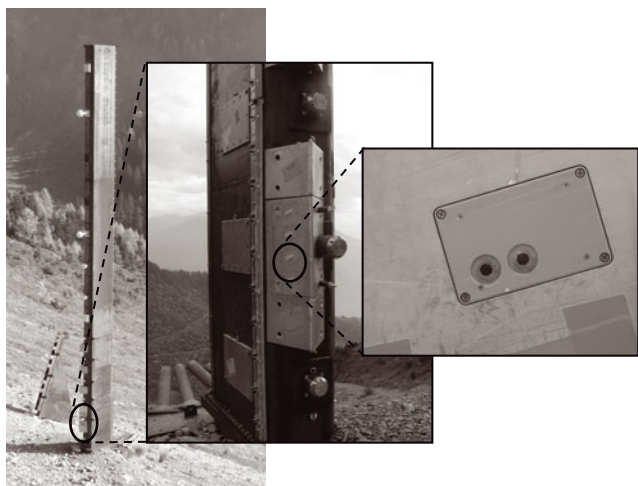
Fig. 1. Optical velocity sensor mounted in flow wedges on the mast at the VdlS test site. Streamwise spacing of the two reflectivity sensors $d = 0.03$ m. The flow direction is from right to left along the line between the two sensors.

powder part of avalanches). Flow heights and the vertical flow structure are recorded by FMCW (frequency-modulated continuous wave) radars mounted flush to the track surface at three locations along the avalanche track.

Near the mast, two additional obstacles are instrumented with pressure gauges to study avalanche impact pressures (Sovilla and others, 2008a,b). On the counter-slope, a manned measurement bunker houses the data-acquisition system and Doppler radars to track the avalanche (front) velocity. For a detailed description of the site, see Issler (1999, 2003) and Sovilla and others (2006, 2008a,b). Typically, two or three artificially released avalanches can be recorded each winter, depending on the snow and weather situation. However, there have been winters in which no avalanches could be released. Continuous and pulsed radar velocity measurements and optical velocity measurements have proven to yield consistent results (Gauer and others, 2007; Rammer and others, 2007). The number of velocity sensors on the mast was recently increased, allowing better resolution of velocity profiles in the shear layer and improved localization of sliding/shear layers.

Optical velocity measurements

Optical velocity sensors are placed 1.25, 1.4, 1.55, 1.7, 2, 3, 4 and 5 m vertically above the ground, flush with the side walls of wedges at the hillside face of the measurement mast (Fig. 1). In what follows, we refer to these vertical heights above the ground by the variable z, treating them as flow-normal heights. That is, $z = 2$ m denotes a flow-normal height $z = 2$ m $\cdot \cos\theta$, where $\theta = 18°$ is the slope inclination at the location of the mast. This convention has been used in previous studies of height dependencies of measures obtained from the VdlS measurement mast (Rammer and others, 2007; Sovilla and others, 2008a,b). For reasons of comparability with previous work, we follow the same convention in this contribution. Furthermore, we use the variable h for flow-normal depths.

Sensors are mounted in wedges to ensure proper contact of the flow with the sensors. The hillside angle of the wedges is 30°, resulting in a mean flow deflection of 15° on frontal impact. The wedges were designed to minimize

flow disturbances around the blunt mast. Placing the sensors directly at the side wall of the mast did not lead to satisfactory results since the flow detached from the mast side walls as snow particles were thrown to the side at the instant of impact at the hillside face of the mast. Although we initially had suspected that an oblique-shock-like flow structure could develop due to the deflection of the avalanche flow at the wedges, similar to the effect outlined by Gray and others (2003) and by Hákonardóttir and Hogg (2005), the wedge construction solved the problem of flow detachment.

The principle of optical velocity measurement requires that the structure of the avalanche flow does not change significantly during the travel of the flow over short distances (Taylor hypothesis). Recording the reflectivity of the passing flow at two points, A and B, with a flow-wise spacing, d, results in two similar time series, $A(t)$ and $B(t)$, which, at a time t_s, have a time lag $\tau(t_s)$. That is, $A(t_s) \approx B(t_s + \tau(t_s))$. From this, the velocity $u(t_s)$ of the passing flow can be estimated to be $u(t_s) = d/\tau(t_s)$. Figure 1 shows an optical velocity sensor mounted on the mast at the VdlS test site, consisting of two reflectivity sensors placed along a flow-parallel line with $d = 0.03$ m.

The optical velocity sensors have been improved and adapted to laboratory-scale, to snow-chute and to real-scale avalanche experiments at VdlS (Kern and others, 2004; Tiefenbacher and Kern, 2004). A discussion of the measurement accuracy is given by McElwaine and Tiefenbacher (2003). The compatibility of optical velocity measurements with Doppler-radar-based velocity measurements was established in a recent study (Rammer and others, 2007). The data analysis procedure will not be repeated in detail here. Instead, we provide a short account of possible problems arising in the analysis of optical velocity sensor data from field experiments which can also be distorted by residual electronic noise.

To determine the time lag between the two sensor signals, $A(t)$ and $B(t)$, of the two reflectivity sensors with a streamwise spacing, d, the correlation integral

$$C^{(t_s)}(\tau) = \int_{t_s - T/2}^{t_s + T/2} dt A(t)\, B(t + \tau) \qquad (1)$$

is computed for a range of time lags, $|\tau| < T/2$, where T is the integration length. For the time lag τ_{max} with $\partial_\tau C(\tau_{max}) = 0$ and $\partial_\tau^2 C(\tau_{max}) < 0$, $C(\tau)$ is maximal and therefore τ_{max} may be assumed to be the time the flow needs to travel the distance, d, between the reflectivity sensors. Accordingly, the flow velocity can be assumed to be $u = d/\tau_{max}$.

Sources of error

In recent analyses of velocity sensor signals, we obtained the velocity time series directly from the correlation function, Equation (1), in some cases employing adjacent averaging of the velocity time series to enhance their readability. This is a reasonable approach to estimate the order of magnitude of velocities (Sovilla and others, 2008a,b) or to compare different velocity measurement techniques (Rammer and others, 2007). However, for a detailed analysis of the internal velocity structure, that is, to extract information regarding the rheological behaviour of the flow, it is necessary to be aware of principal constraints and inherent ambiguities in the measurements.

Spurious velocities due to noise

It is important to note that by determining the velocity as sketched above, we interpret the reflectivity time series as representations of the spatial pattern of the flow passing the flow-wise displaced sensors and relate the time lag, τ, obtained from the correlation integral, Equation (1), to the time the flow pattern needs to travel the flow-wise distance, d. A major source of error in the determination of the flow velocity is that the correlation integral, $C(\tau)$, may have multiple maxima that are not necessarily related to the passing flow structure. Accordingly, the choice of the 'wrong' τ_{max} may result in a misleading flow velocity, as shown in Figure 2. We demonstrate this effect by a very simple example.

Consider two identical, periodic signals with overlaid (periodic) distortion which, for reasons of simplicity, is assumed to be a harmonic of the signal:

$$A(t) = B(t) = a\,e^{i\omega t} + b\,e^{im\omega t}, \quad m = 2, 3, \ldots, \quad (2)$$

where a and $b < a$ are the amplitudes and ω and $m\omega$ are the frequencies of the signal and the distortion, respectively. For simplicity, we set $t_s = 0$ and assume the signal to extend from $-\infty$ to $+\infty$. The correlation integral then is

$$C(\tau) = \int_{-T/2}^{T/2} dt \left(a\,e^{i\omega t} + b\,e^{im\omega t}\right)\left(a\,e^{i\omega(t+\tau)} + b\,e^{im\omega(t+\tau)}\right)$$

$$= \int_{-T/2}^{T/2} dt\, a^2\,e^{i\omega(2t+\tau)} + ab\,e^{i\omega[(m+1)t+m\tau]}$$

$$+ ab\,e^{i\omega[(m+1)t+\tau]} + b^2\,e^{im\omega(2t+\tau)}. \quad (3)$$

Consider the first term in the second line of Equation (3), which describes the (auto)correlation of the signal and, as $a \gg b$, normally dominates the correlation integral (we may replace $T/2$ with $T \gg 2\pi/\omega$ without loss of generality):

$$C_a^{(t_s=0)}(\tau) = \int_{-T}^{T} dt\, a^2\,e^{i\omega(2t+\tau)}$$

$$= a^2 e^{i\omega\tau} \left[\frac{e^{2i\omega t}}{2i\omega}\right]_{-T}^{T}$$

$$= -\frac{ia^2 e^{i\omega\tau}}{2\omega} 2i\sin(2\omega T). \quad (4)$$

Now consider the real parts of $C_a(\tau)$ and its derivatives:

$$\mathcal{R}(C_a(\tau)) = \frac{a^2}{\omega}\cos(\omega\tau)\sin(2\omega T),$$

$$\mathcal{R}(\partial_\tau C_a(\tau)) = -a^2\sin(\omega\tau)\sin(2\omega T),$$

$$\mathcal{R}(\partial_\tau^2 C_a(\tau)) = -a^2\omega\cos(\omega\tau)\sin(2\omega T). \quad (5)$$

Demanding $\mathcal{R}(\partial_\tau C_a(\tau_{max})) = 0$ and $\mathcal{R}(\partial_\tau^2 C_a(\tau_{max})) < 0$, maxima of $\mathcal{R}(C_a(\tau))$ are present for $\tau_{max} = 2\pi k/\omega$, where $k = 0, 1, \ldots$. If $a \gg b$, maxima related to correlations of the signal and the noise (second and third terms in Equation (3)) or to noise–noise correlation (fourth term) will be negligible. This situation, however, dramatically changes if the signal–noise ratio decreases. In the extreme case $a/b \to 0$, the signal even disappears and the correlation
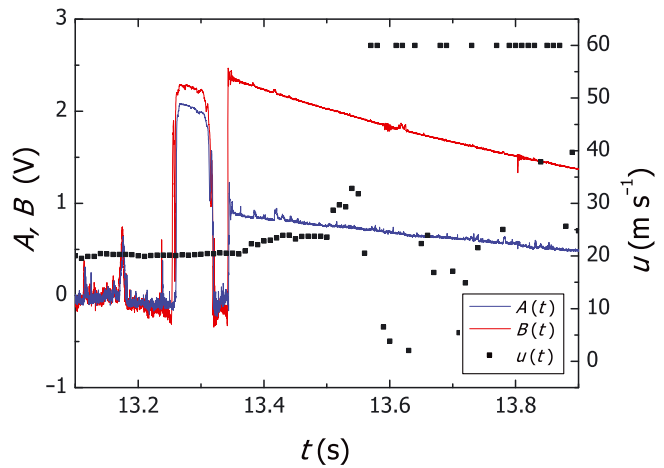

Fig. 2. Raw reflectivity signals, $A(t)$ and $B(t)$, from a velocity sensor at the Vdls mast (sampled with 20 kHz) and velocities (squares) computed directly from the time lag where the correlation integral with $T = 0.4\,s$ is maximal. (Note that each of the two reflectivity sensors that make up a velocity sensor is connected to an individual amplifier. Due to rough environmental conditions, these amplifiers are subject to varying drifts and offsets that can result in signals of similar fluctuation structure but varying and different amplitudes. For this reason, the reflectivity data have to be pre-processed before performing a correlation analysis: for each correlation time window, we subtract the mean over the correlation time window from the data and scale these fluctuations by their standard deviation over the correlation window (Tiefenbacher and Kern, 2004). However, in this figure, we plot the raw sensor signals to demonstrate the collapse of the signal–noise ratio which is not visible in time series of scaled fluctuations.)

integral, Equation (3), collapses to the fourth term, that is to the noise–noise correlation:

$$C_b(\tau) = \int_{-T}^{T} dt\, b^2\,e^{im\omega(2t+\tau)}$$

$$= -\frac{ib^2 e^{im\omega\tau}}{2m\omega} 2i\sin(2m\omega T). \quad (6)$$

Similar to the signal–signal correlation, we find

$$\mathcal{R}(C_b(\tau)) = \frac{b^2}{m\omega}\cos(m\omega\tau)\sin(2m\omega T),$$

$$\mathcal{R}(\partial_\tau C_b(\tau)) = -b^2\sin(m\omega\tau)\sin(2m\omega T),$$

$$\mathcal{R}(\partial_\tau^2 C_b(\tau)) = -b^2 m\omega\cos(m\omega\tau)\sin(2m\omega T), \quad (7)$$

which, by the conditions $\mathcal{R}(\partial_\tau C_b(\tau_{max})) = 0$ and $\mathcal{R}(\partial_\tau^2 C_b(\tau_{max})) < 0$, yields maxima at $\tau_{max} = 2\pi k/m\omega$. Recall that the noise is assumed to be of higher frequency than the signal (mth harmonic). Consequently, in the case of $A(t)$ and $B(t)$ being the signals of the reflectivity sensors of our set-up, falsely interpreting the noise–noise correlation time lags as related to passing flow pattern results in velocities m times as high as the velocities derived from the signal–signal correlation.

In our measurements, the structure of the reflectivity signals is not as simple as the simple periodic and it would rather have to be described in terms of its Fourier or wavelet spectra. However, if modes of the signal and noise spectra behave in a similar way, as outlined above, then unrealistically high spurious velocities can be encountered. This is important as some noise may persist even after
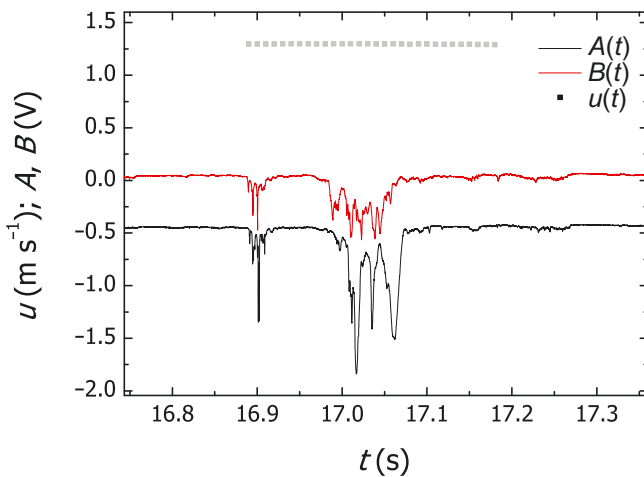
Fig. 3. Example of disjoint signal packages with a duration shorter than the integration length, $T = 0.4\,\text{s}$, of the correlation function, causing apparently constant velocity (grey dots).

filtering. This noise was observed to be periodic, probably due to unintended inductivities in the amplifier electronics. Note that in the case of missing reflectivity signals, even periodic bit-noise will lead to false velocities.

Figure 2 shows such a situation. Once the reflectivity signal decays, the correlation analysis yields unrealistically high velocities, as soon as the integration length of the correlation integral does not extend over parts of the signals with a high signal–noise ratio. The example shown in Figure 2, $T/2 = 0.2\,\text{s}$, reveals that the 'true' velocity persists for $0.2\,\text{s}$ after the signal–noise ratio has collapsed. The apparent decay of the signal is due to the transient behaviour of the signal amplifiers.

The above considerations can only be applied if signal and noise can clearly be distinguished, which might not be the case for fast dilute flows where both the amplitudes and timescale of noise and signal may be of the same order of magnitude.

Correlation lengths

Finding the correct maxima is closely related to the task of choosing an appropriate length of the correlation integral. For slow flows, the integration length must capture a part of the real flow structure long enough to ensure that a maximum related to the flow structure (i.e. related to long-timescale structures in the reflectivity time series) is found. High-frequency noise can disrupt the search for maxima before a maximum related to the flow structure is found. For a flow with mean velocity, u, consisting of particles with a typical size, $\bar{r}$, and a flow-wise spacing, d, of the two reflectivity sensors, A and B, the integration length, T, of the correlation integral must satisfy

$$\frac{T}{2} \geq \frac{d + \bar{r}}{u} \tag{8}$$

to ensure overlap of the signals and to avoid capturing noise maxima. This is especially important for slow flows of coarse snow lumps. Typical slow-flow conditions for snow avalanches in VdlS are $u \approx 1\,\text{m s}^{-1}$, $d = 0.03\,\text{m}$ and $\bar{r} = 0.05\,\text{m}$, requiring $T \geq 0.15\,\text{s}$.

Maximum acceleration

Erratic high or low velocities may also occur in time series obtained by the correlation procedure, due to non-similarities of the signals (caused by slightly different lighting angles of the passing crystalline snow structures). These erratic values can be excluded by a simple argument: correlation integrals are evaluated at discrete times, $t_\text{s} = n\Delta t$, $n = 0, 1, \ldots$, yielding a discrete velocity time series. The local acceleration,

$$a_\text{eff} = \frac{u\left(t_\text{s}^{(n)}\right) - u\left(t_\text{s}^{(n+1)}\right)}{\Delta t}, \tag{9}$$

within a dense avalanche flow between two time points, $t_\text{s}^{(n)} = n\Delta t$ and $t_\text{s}^{(n+1)} = (n + 1)\Delta t$, must not exceed an upper bound, a_max. Given the fact that typical velocity fluctuations even in turbulent flows are an order of magnitude smaller than the mean flow velocity, $\bar{u}$, $a_\text{max} = \bar{u}/(\alpha\Delta t)$, $1 < \alpha < 10$ may be estimated to be a fair limit on the possible local accelerations in the flow. The argument of constrained acceleration makes use of the fact that quasi-discontinuities in the particle velocities, such as encountered in dilute flows of hard-sphere granular media, are very unlikely to occur in the dense flows considered here.

Elongated peaks

Determination of the velocity by the correlation integral (Equation (1)) at a time t_s involves signal information contained in the time interval $[t_\text{s} - T/2, t_\text{s} + T/2]$, leading to an inherent averaging of the signal. This may produce apparently constant velocities over the time interval, if the signals are disjoint, as in the dilute-flow regime, where the flow passing the sensor is no longer quasi-laminar so that only short coherent signals, according to mean-flow-parallel eddy components of the turbulent flow or to dilute snow particles, are encountered by the sensors. Figure 3 shows an example of such a short-duration coherent signal peak.

The integration length, T, typically exceeds the time-step, Δt_s, between the discrete times where the velocity is computed. A frequent choice for low- to medium-velocity flows is $\Delta t_\text{s} = 0.01\,\text{s}$ and $T = 0.4\,\text{s}$. Isolated signal peaks, extending over a short time interval, $\Delta t_\text{p} < T$, which is centered at t_p, therefore dominate the correlation function as long as $[t_\text{p} - \Delta t_\text{p}/2, t_\text{p} + \Delta t_\text{p}/2] \cap [t_\text{s} - T/2, t_\text{s} + T/2] \neq 0$, leading to the same time lag, τ, for all t_s matching this condition. Disjoint signal peaks are therefore 'smeared out', leading to apparently constant velocities over time intervals of the order of magnitude of the integration length of the correlation integral.

Smoothing

The nature of the correlation procedure implies an inherent averaging of the reflectivity signals over the integration interval of the correlation function. However, even under these conditions, additional smoothing of the final velocity time series by adjacent averaging may be useful to improve the readability of the velocity time series. However, the smoothing interval, Δt_sm, must not exceed the timescale for the passing of structures with a scale of interest, r_i, i.e. $\Delta t_\text{sm} \leq r_\text{i}/\bar{u}$. Figure 4 shows a velocity time series of a dense, slow avalanche (avalanche No. 8448; see below) that did not detach from the sensors and passed the error checks so that only a few points of noise velocity had to be eliminated. The time series has been smoothed by adjacent averaging over
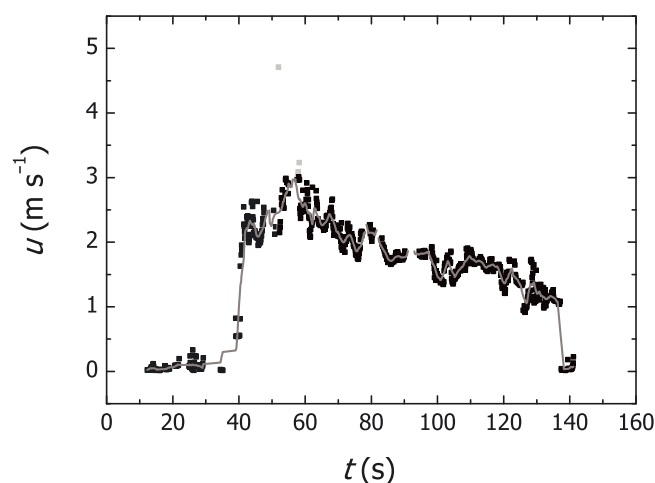
Fig. 4. Example of a velocity time series of an avalanche passing a sensor at the mast, 3 m above the ground (black squares). Data are smoothed over a time interval of 2 s (continuous curve). Only a few data points related to erroneous velocities were rejected (grey dots, e.g. at $t = 50$ and $60\,s$).

a time window, $\Delta t_{sm} = 2\,s$, setting the scale of interest to $r_i \geq 3\text{–}6\,m$.

Mechanical sources of error

The signals recorded by the velocity sensors can be damped by snow frozen at the sensors. This effect can even inhibit any signal detection. The signals can also be significantly blurred by detachment of the flow passing the sensors. Furthermore, movements due to settling of the snow cover as it is overrun by the avalanche or the vibrations of the mast during an avalanche may produce misleading signals from sensors situated in the overrun snow cover.

MEASURED AVALANCHES

In this section, we outline the characteristics and weather conditions of the three avalanche events used in this analysis. Weather data were collected by an automatic weather station located at the ridge of Crêta Besse, directly above the release zone of the VdlS avalanche path.

Avalanche No. 7226, 21 January 2005

On 21 January 2005 at 1500 h, an avalanche was released naturally from the release zone 'Crêta Besse II'. (For a situation map of Crêta Besse II, see Issler (1999) or Sovilla and others (2008b).) Moderate snowfall over several days had added ~15 cm of new snow to the ~1 m thick snow cover in the release zone. Temperatures at release were measured to be about −4°C after a significant temperature rise from −14°C, which also affected the snow cover: snow-surface temperatures had been rising from −25 to −4°C. At the time of the release, there was a moderate westerly wind with a mean velocity of ~10 m s⁻¹ and maxima of up to 20 m s⁻¹. The temperatures in the run-out zone were ~0°C. The measurement system was automatically triggered by geophones, and the recorded data indicate a dry, dense flowing avalanche that may be characterized by two parts: a high-speed phase in which velocity variations and considerable shear were present, and a low-speed flow ('tail').
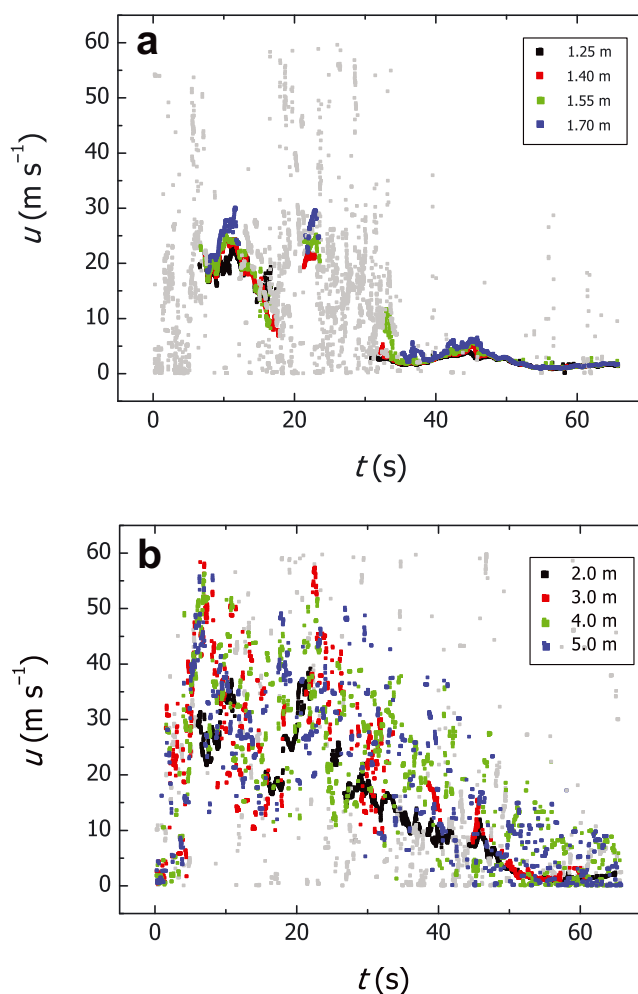

Fig. 5. Velocity time series of avalanche No. 7226. (a) Extracted from lower sensors (at 1.25, 1.4, 1.55 and 1.7 m above ground level). Grey squares indicate data which were rejected due to partial flow detachment of the dense flow and due to the maximum acceleration argument. (b) Extracted from higher sensors (at 2, 3, 4 and 5 m above ground level). Blurred signals indicate dilute flow. (Note that the offset of our time base compared to that of the corresponding plots in Sovilla and others (2008a) is −64 s, i.e. our $t = 0$ corresponds to their $t = 64\,s$.)

Figure 5 shows time series of flow velocities above and below 2 m elevation from the ground. Velocities recorded in flow heights >2 m are related to the dilute component of the fast, dry flow part of the avalanche. The fact that non-zero velocities were recorded at all sensors indicates that the basal sliding/shear layer of the avalanche was situated below the lowest sensor at $z = 1.25\,m$. Note the considerable flow height despite the small amount of new snow. It appears that the fracture of the releasing snow slab occurred in lower layers of the old snow cover and was related to the temperature rise in the release zone. The considerable flow height might also be due to erosion and entrainment of snow. However, as no photogrammetric data could be collected for this naturally released avalanche, both explanations remain speculative.

Avalanche No. 816, 6 March 2006

Between 2 and 4 March 2006, a heavy snowfall (120 cm of new snow) was accompanied by a strong increase in temperature (~12°C). The snowline retreated up to >2000 m a.s.l. On 5 March, the temperature rapidly dropped
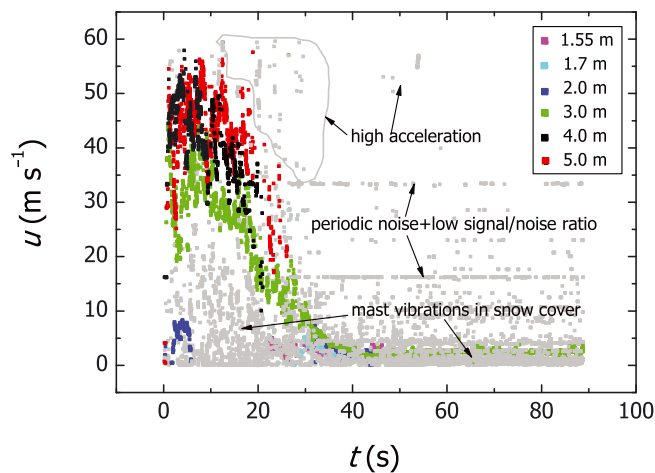
Fig. 6. Velocity time series of avalanche No. 816. Blurred signals indicate partial detachment of flow from the optical sensors and turbulent motion; grey squares indicate rejected data. Reasons for rejecting are indicated for several of the rejected data points.

from -4 to $-16°C$ in the release zone. The weather cleared and an avalanche was released artificially by explosives at 1000 h on 6 March.

The released avalanche was of mixed dry type (i.e. a dry dense avalanche with a significant powder cloud) and exhibited shear and velocity variations in time. Figure 6 shows a plot of velocity time series from the velocity sensors at levels ≤ 2, 3, 4 and 5 m above the ground. The signals are blurred, indicating that the flow has detached from the mast and/or the avalanche impacted the measuring pylon from the side.

Avalanche No. 8448, 1 March 2007

After a period of cloudy weather with relatively high temperatures around the freezing point, snowfall started around midday on 1 March 2007, accumulating 0.6–0.7 m of new snow on the existing 2–3 m thick snow cover in the release area. The snowfall lasted until the early morning of 2 March. During the snowfall, there was a moderate wind
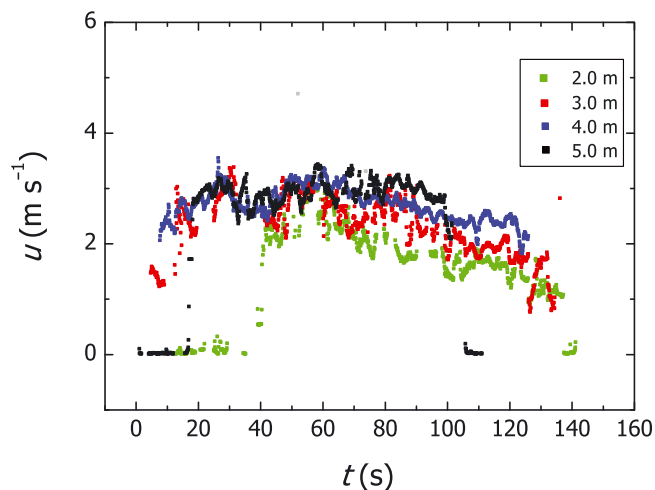

Fig. 7. Velocity time series of avalanche No. 8448. The delayed onset of the signal at $z = 2$ m indicates erosional processes.

from westerly directions with speeds up to $10\,\mathrm{m\,s^{-1}}$. The temperature was about $-4°C$ in the release zone, and around or slightly above $0°C$ in the run-out zone. After ~ 0.4 m of new snow had accumulated, an avalanche was released spontaneously at 2119 h. The avalanche exhibited typical wet, dense, slow-flow and steady-flow behaviour. The basal shear/sliding layer could clearly be identified and, due to the relatively steady flow behaviour (Fig. 7), a velocity profile based on a 40 s time average could be extracted from the velocity time series.

MEASURED SHEAR RATES

The optical velocity measurements were used to determine the shear rates of the flow. For simplicity, we assume the avalanche to be a (locally) steady simple shear flow $\boldsymbol{u} = u(z)\hat{e}_x$, where x denotes the downstream and z the flow-normal direction, and write the shear rate as

$$\gamma = \partial_z u(z). \tag{10}$$

We write $u(z)$ as $u(z) = \bar{u}(z) + \delta u$ where $\bar{u}(z) = \langle u(z)\rangle_t$ is the time average over an averaging interval Δt_{av}:

$$\langle \cdots \rangle_t = \frac{1}{\Delta t_{av}} \int_{t-\Delta t_{av}/2}^{t+\Delta t_{av}/2} \cdots \mathrm{d}t'. \tag{11}$$

We denote the standard deviation of $u(z)$ by $\delta u(z) = \sqrt{\langle (u(z) - \bar{u}(z))^2\rangle_t}$. As we use time series that have passed the outlined error checks, we neglect the influence of residual measurement errors and interpret the standard deviation, $\delta u(z)$, as a measure of the magnitude of actual velocity variations around the mean.

To estimate mean shear rates, we define depth averaging as

$$\langle \cdots \rangle = \frac{1}{h_s - h_b} \int_{h_b}^{h_s} \cdots \mathrm{d}z, \tag{12}$$

where h_b and h_s are the estimated flow-normal elevations of the running surface ('base') and the surface of the considered shear zone, respectively.

The velocity variations, δu, impose an uncertainty, $\delta \dot{\gamma} = \left[\sqrt{(\delta u(h_s))^2 + (\delta u(h_b))^2} \right] / (h_s - h_b)$, on the estimates of the mean shear rate, $\dot{\gamma} = \langle \gamma \rangle = (u(h_s) - u(h_b)) / (h_s - h_b)$. In what follows, we give estimates of the mean shear rates in the form $\dot{\gamma} = \langle \gamma \rangle \pm \delta \dot{\gamma}$.

We use the terms 'sliding surface' or 'running surface' to describe the surface of discontinuous transition between the non-moving and moving snow at the base of the avalanche. That is, at this surface the avalanche has a non-zero slip velocity, denoted by u_0. Below this surface there is no movement of snow. This terminology is required to compare the measurements with flow models, which usually assume a sliding surface. If the avalanche has no slip velocity, but a gradual increase in velocity, we term the layer at which $u_0 = 0$ the 'basal interface'. The region of increasing velocity above the running surface or the basal interface is termed 'shear layer'. Usually this region is characterized by the largest shear rates within the flow. The height of the shear layer is defined by a sudden decrease in the shear rates, observed in the measurements. Regions of low shear rate, compared with the shear layer, are termed 'plug flows'.

Note that generating velocity profiles and averaged quantities requires time windows in which the velocity data match the quality criteria jointly for all sensors. This constraint is reflected in the fact that we could generate fewer velocity profiles near the front than towards the transitional and tail regions of the avalanches.

Avalanche No. 7226

Three time intervals could be found within the measurements which passed the stringent data-analysis requirements outlined above: [10 s, 12 s] (front), [44.8 s, 44.9 s] (tail with dense shear flow) and [55 s, 57 s] (tail with plug flow). In these intervals the velocity time series exhibit approximately steady velocities modulated by velocity fluctuations. All sensors provided non-zero velocity values, indicating that the running surface was located below the level of the lowest velocity sensor, at $z = 1.25$ m above the ground. Using data from pressure sensors mounted at the mast (Sovilla and others, 2008a) in the time interval [10 s, 12 s], the running surface was located $\sim$0.6–0.7 m above the ground. Figure 8 depicts the three measured velocity profiles.

From the time series (Fig. 5), the front part of the avalanche can be characterized as a flowing avalanche with a powder/suspension cloud. The change from coherent to scattered signals between 1.7 and 2 m above the ground appears to be related to the transition between the dense flow part and the powder cloud. Using pressure data, Sovilla and others (2008a) located this transition at flow heights $z > 2.5$ m, which is consistent with the velocity measurements.

The presence of velocity profile inversions with lower velocities immediately above the transition might indicate the passage of large-scale eddy-like structures at the surface of the flowing avalanche. As the avalanche passes the mast, the overall velocity decreases. The dense flow undergoes a transition from a highly sheared front to a slow-moving, dense plug-flow behaviour at the tail.

Dense flows are characterized by a more-or-less coherent structure of the raw signal and of the derived velocity time series. In the time series of the lower sensors, these coherent parts were disrupted by sequences of disjoint time series with strong fluctuations, that did not match the maximum acceleration condition. As this effect occurred on all lower heights $z \leq 2$ m, we interpret it as a detachment of the flow from the sensors rather than as a transition to a different flow regime. However, as the impact pressure (Sovilla and others, 2008a, fig. 9) drops at these times, one also could interpret this as a transient dilute-flow phase extending from lower ($z \leq 2$ m) to higher ($z > 2$ m) flow heights. Note that we did not apply the maximum acceleration argument for the higher flow layers as they were dilute at all times. We confine our discussion to the coherent and dense flow parts.

In the time interval [10 s, 12 s], coherent reflectivity signals yield approximately constant velocities with weak, small-scale fluctuations for flow depths $z \leq 2$ m (Fig. 8). Assuming the flow reaches down to the ground, $z = 0$, the mean shear rate, $\dot{\gamma}$, for the lowest layer $z < 1.25$ m is $\sim$17.7 $\pm$ 1.3 s^{-1}. Locating the basal surface at $z = 0.6$ m, the mean basal shear rate is twice as high, $\dot{\gamma} = 34.1 \pm 2.5$ s^{-1}.

The mean shear rate between 1.7 and 2 m is about $\dot{\gamma} = 24.9 \pm 7.0$ s^{-1} and decreases to $\dot{\gamma} = 13.7 \pm 5.3$ s^{-1} between 1.25 and 1.7 m. This observation differs from that of Sovilla and others (2008a) in the time interval [5 s, 7 s] (their [69 s, 71 s]), who did not observe an increase of the shear rate with z. This is due to the fact that the shapes of velocity
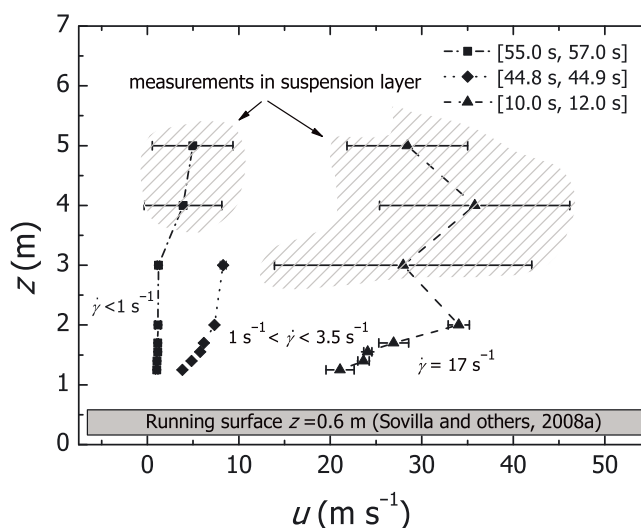

Fig. 8. Velocity profiles and shear rates in avalanche No. 7226. Three time periods could be analysed: behind the front (10.0 s $\leq t \leq 12.0$ s), dense shear flow (44.8 s $\leq t \leq 44.9$ s) and plug-flow tail (55.0 s $\leq t \leq 57.0$ s). The mean shear rates decrease from front to tail. (Lines are just eye-guides and do not imply interpolation. Error bars indicate the standard deviation of velocity variations. Note that the data allow no decision on whether the avalanche was sliding at the base or whether there was a thin shear layer above the base without sliding.)

profiles vary in the avalanche flow and cannot be considered steady on longer timescales, especially for time intervals shortly after the passage of the avalanche front. Averaging time intervals must be chosen to correspond to a timescale on which the flow may be estimated to be locally steady.

For the dense flow phase in the time interval [44.8 s, 44.9 s] (Fig. 8), the shear rates lay in the range $1 \leq \dot{\gamma} \leq 3.5$ s^{-1} and decrease with height above the ground. Meaningful signals above $z > 3$ m could not be obtained. This might be due to the decelerating snow–air suspension above the flowing avalanche.

In the time interval [55 s, 57 s], which is related to the tail of the avalanche, a plug-flow velocity profile is present (Fig. 8). The measured shear rates are $0 \leq \dot{\gamma} \leq 1$ s^{-1}. Coherent velocity measurements are obtained up to $z = 3$ m. The underlying sliding/shear layer must be situated below the lowest velocity sensor at $z = 1.25$ m. The strongly scattered velocity signal at the 4 and 5 m sensors might again be caused by decelerated remainders of the suspension layer of the avalanche.

Avalanche No. 816

The measured velocity profiles for avalanche No. 816 (Fig. 9) show the evolution from a fast-moving dry flowing avalanche with suspension layer (front, time interval [2.1 s, 5.4 s]) to a decelerating dense shear flow ([32.4 s, 33.15 s]) and, finally, to a plug-like flow at the tail of the avalanche ([40.4 s, 42.5 s]).

For times $t_s < 5.4$ s, velocity measurements were recorded by all the sensors located >2 m above the ground. Therefore the running surface or basal interface at the front must be located between the sensors at 2 and 1.7 m. For times $t_s > 20$ s, the signals of sensors at 4 and 5 m elevation decay but signals are recorded by sensors located between 1.55 and 3 m. This can be interpreted as indicating that the flow
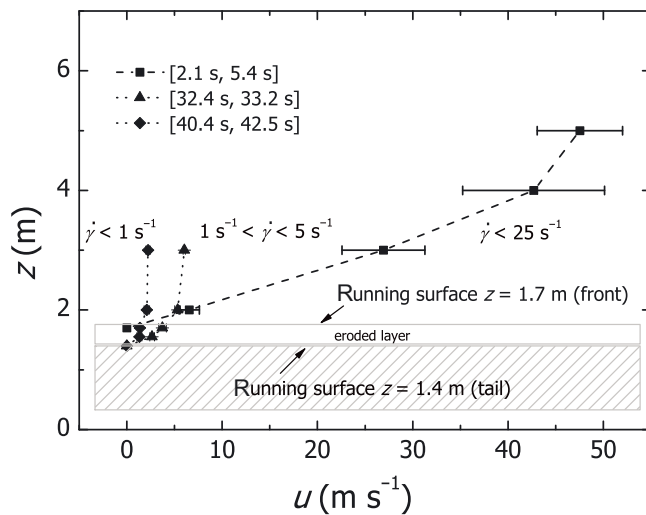
Fig. 9. Velocity profiles and shear rates in avalanche No. 816. Three time periods could be analysed: front ($2.1\,\mathrm{s} \leq t \leq 5.4\,\mathrm{s}$), decelerating dense shear flow ($32.4\,\mathrm{s} \leq t \leq 33.2\,\mathrm{s}$) and tail ($40.4\,\mathrm{s} \leq t \leq 42.5\,\mathrm{s}$). The mean shear rates decrease from front to tail. Error bars indicate the standard deviation of velocity variations. Note that the running surface indicated in the plot could also be a basal interface.
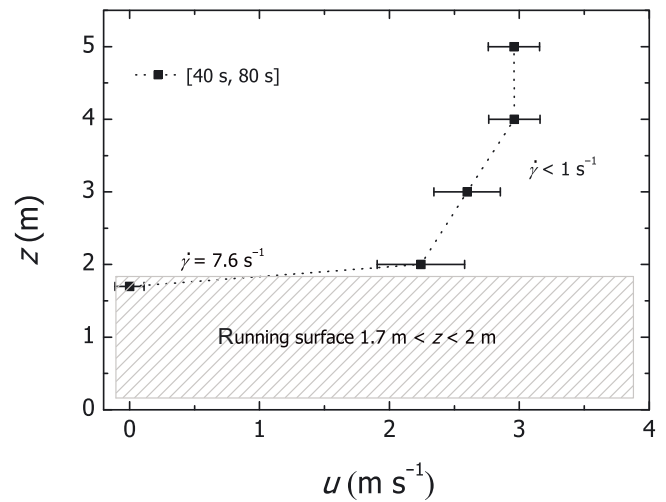

Fig. 10. Velocity profile and shear rates extracted from the velocity time series of avalanche No. 8448 (see Fig. 7). One long time period could be analysed at the tail ($40.0\,\mathrm{s} \leq t \leq 80.0\,\mathrm{s}$). Error bars indicate the standard deviation of velocity variations. Note that the running surface indicated in the plot could also be a basal interface.

heights at the tail are decreasing. In addition, it appears that the running surface is moving downwards. Note that the eroded layer depth indicated in Figure 9 is the layer thought to be eroded by the avalanche after the passing of the first front at $t \geq 2.1\,\mathrm{s}$. It is likely that significant erosion of the uppermost snow layers occurred earlier at the first front of the avalanche, i.e. for $t < 2.1\,\mathrm{s}$.

The velocity profile at the front (Fig. 9) is characterized by shear rates of up to $20\,\mathrm{s}^{-1}$ between $z = 2$ and $4\,\mathrm{m}$. There is a strong scatter in the velocity signals in this region. Accordingly, the transition between dense flow and suspension layer appears to be situated between 2 and $3\,\mathrm{m}$. The basal interface/running surface is located near $z = 1.7\,\mathrm{m}$ and thus the flow height of the dense avalanche is $\sim 1\,\mathrm{m}$.

For times $t > 20\,\mathrm{s}$, signals from the upper flow layers decay, and, on decelerating, the avalanche shows a more dense flow behaviour. In the time interval $[32.4\,\mathrm{s}, 33.15\,\mathrm{s}]$, the mean shear rate is $\dot{\gamma} = 4.0 \pm 0.1\,\mathrm{s}^{-1}$, whereas later in the flow, there are only two confined shear layers, between $z = 1.4$ and $1.55\,\mathrm{m}$ and between $z = 1.7$ and $2\,\mathrm{m}$, with shear rates $\dot{\gamma} = 18.6 \pm 1.8$ and $7.6 \pm 3.3\,\mathrm{s}^{-1}$, respectively.

Avalanche No. 8448

From the plot of the velocity time series (Fig. 7), we observe that this avalanche exhibits a decelerating dense shear flow behaviour at low mean flow velocity. Though not strongly varying on a long timescale, on a short timescale of 2–5 s the flow velocities vary considerably, indicating a surge- and wave-like motion of the avalanche flow. We note the delayed onset of the velocity signal at $z = 2\,\mathrm{m}$, indicating erosion. As the mean flow velocity only slightly decreases over a long time period, we were able to extract a velocity profile (Fig. 10) by averaging the time series over an extended time period $[40\,\mathrm{s}, 80\,\mathrm{s}]$.

The velocity profile of this slow-moving wet snow avalanche (Fig. 10) indicates no flow at $1.7\,\mathrm{m}$ height, $u(z = 1.7\,\mathrm{m}) = 0\,\mathrm{m\,s}^{-1}$, and $u(z = 2.0\,\mathrm{m}) = 2.3 \pm 0.3\,\mathrm{m\,s}^{-1}$. Therefore, the shear layer is located between 1.7 and $2\,\mathrm{m}$.

Large shear deformations are thus localized in this $0.3\,\mathrm{m}$ narrow near-base flow layer. The shear rate is at least $\dot{\gamma} = 8.0 \pm 1.3\,\mathrm{s}^{-1}$. This value is a lower bound for the actual shear rate, as the spatial resolution of the velocity measurement is $\Delta z = 0.3\,\mathrm{m}$. A slip velocity, $u_0 = 2.3 \pm 0.3\,\mathrm{m\,s}^{-1}$, is also consistent with the measurements. Above this high shear layer (or sliding surface), the velocity increase between 2 and $4\,\mathrm{m}$ is just $0.7\,\mathrm{m\,s}^{-1}$, indicating a shear rate of only $\dot{\gamma} = 0.38 \pm 0.21\,\mathrm{s}^{-1}$. Between 4 and $5\,\mathrm{m}$, the shear rate is even lower ($\dot{\gamma} = 0.01 \pm 0.29\,\mathrm{s}^{-1}$) and the motion characteristics are close to those of a pure plug flow.

Snow-chute experiments with flow heights of $\sim 0.5\,\mathrm{m}$ have revealed considerable slip velocity at the flow base and a relatively narrow basal shear layer with shear of the order of magnitude of $\dot{\gamma} \approx 50\,\mathrm{s}^{-1}$. It is not yet clear whether this behaviour is due to the special conditions of the experimental chute. Molten and refrozen shear planes are often found in avalanche deposits (Kern and others, 2004), indicating that a discrete sliding surface often exists. Such sliding surfaces are thought to be mostly formed at the tail of the avalanche. The velocity measurements of avalanche No. 8448 provide some experimental evidence to support this idea.

MEAN SHEAR RATE, DISCHARGE AND VARIATIONS FROM THE MEAN VELOCITY

In this section, we attempt to generally characterize the flow behaviour and to find a relationship between the measured mean shear rate and the mean flow discharge.

We study depth-averaged, or 'mean', values because the spatial resolution of the optical sensors does not yet allow detailed z-dependent statements regarding the flow rheology. Our motivation is to judge whether the measurements provide consistent results from the head to the tail of the avalanche.

As indicated above, the shear rates, $\dot{\gamma}(z)$, can be extracted from the time-averaged velocity profiles, $\bar{u}(z) = \langle u(z) \rangle_t$ (Equation (11)). Using the time-averaged velocities in the dense layer between h_b and h_s, we can then find the mean shear rate between the running surface and the surface of

Table 1. Results of depth-averaging the velocity measurements

Avalanche No.	Δt_{av}	$\dot{\gamma}$	$\langle \delta u \rangle$	$\langle \bar{u} \rangle$	h	Q	Re	Fr
	s	s^{-1}	m s^{-1}	m s^{-1}	m	m^2 s^{-1}		
7226	[10, 12]	25.6 ± 0.8	0.94 ± 0.14	20.9 ± 1.5	1.3 ± 0.2	27.7 ± 2.0	103 ± 16	5.9 ± 0.4
7226 *	[44.8, 44.9]	3.6 ± 0.2	0.17 ± 0.11	5.9 ± 0.4	2.3 ± 0.2	13.5 ± 2.3	4.8 ± 0.8	1.3 ± 0.1
7226	[55, 57]	0.5 ± 0.1	0.13 ± 0.02	1.0 ± 0.2	2.3 ± 0.2	2.3 ± 0.4	0.14 ± 0.05	0.22 ± 0.04
816 †	[2.1, 5.4]	14.7 ± 1.5	5.0 ± 0.9	37.5 ± 3.7	3.1 ± 0.3	118 ± 12	140 ± 30	6.9 ± 0.7
816	[32.4, 33.15]	4.0 ± 0.1	0.19 ± 0.03	5.4 ± 1.0	1.5 ± 0.2	8.2 ± 1.5	5.9 ± 2.3	1.4 ± 0.3
816	[40.4, 42.5]	1.5 ± 0.1	0.24 ± 0.06	2.0 ± 0.4	1.5 ± 0.2	3.1 ± 0.5	0.9 ± 0.3	0.5 ± 0.1
8448	[72, 74]	0.95 ± 0.05	0.09 ± 0.02	2.6 ± 0.2	3.1 ± 0.3	8.3 ± 0.5	0.7 ± 0.1	0.50 ± 0.05

*This data point is not considered because Δt_{av} is too short.
†This data point is not considered because the flow is almost entirely dilute.

the dense shear flow, $\dot{\gamma} = \langle \gamma(z) \rangle \pm \delta\dot{\gamma}$ (Equation (12)). The results of the depth averaging of time-averaged profiles are presented in Table 1.

As we do not have any information about the velocities between the lowest sensor and the $u = 0$ surface at h_b, we use a linear interpolation between $u(h_b) = 0$ and the velocity at the lowest sensor position as a crude approximation for estimating the mean quantities. As we cannot determine whether there is basal slip, we assume $u(h_b) = 0$ for all cases. Raw estimates of the basal interface location, h_b, are indicated in Figures 8–10.

The time-averaging intervals of the velocity profiles are confined to the intervals judged to provide meaningful results according to our previous error considerations. For this reason, the time-averaging intervals vary to some extent. Meaningful comparisons, however, need to take into account velocity profiles averaged over comparable time intervals, Δt_{av}. Accordingly, we have to exclude the velocity profile in the middle part of avalanche No. 7226 which is a snapshot over a very short time interval, [44.8 s, 44.9 s] (Table 1). The averaging intervals of the other velocity profiles extend over durations on the scale of seconds. We specifically used $\Delta t_{av} = 2$ s over the interval [72 s, 74 s] to compute the time-averaged characteristics of avalanche No. 8448. Furthermore, we do not include the initial part of avalanche No. 816 ([2.1 s, 5.4 s]) as the flow was dilute over almost the complete flow depth.

The time- and depth-averaged flow velocity allows us to calculate the volumetric discharge, Q, per unit flow width for the dense flowing part

$$Q = h\langle \bar{u} \rangle, \qquad (13)$$

where $h = h_s - h_b$ is the dense flow depth. (The location of the dense flow surface, h_s, was estimated from the structure of the velocity time series: the upper boundary of the dense flow is estimated to be located between the uppermost of the sensors providing a coherent velocity signal and the lowest of the sensors that produce a disjoint signal, indicating dilute flow. That is, the transition between dense and dilute flow is indicated by a significant rise in the standard deviations of the time-averaged velocities (error bars in Figs 8–10). Note that Sovilla and others (2008a) directly measured the dense flow height, h, using flow height switches and estimate it from pressure measurements. Their values are compatible with those extracted from the velocity data in this study.) Furthermore, we can estimate the Froude and Reynolds

numbers, Fr and Re. The Froude number is

$$\mathrm{Fr} = \frac{\langle \bar{u} \rangle}{\sqrt{gh\cos\theta}}, \qquad (14)$$

with g denoting gravitational acceleration, and $\theta = 18°$ the slope inclination at the mast location. To estimate the Reynolds number of the dense flow, we note that avalanche flows are obviously non-Newtonian and adopt the effective viscosity approach, $\eta_{eff} \approx \sigma_s / \dot{\gamma}$, where σ_s is the shear stress at the running/sliding surface (see Kern and others, 2004, and references therein). Though the considered avalanche flows are not steady, we grossly assume the basal friction to be balanced by gravitational forces. As a further crude approximation, we neglect normal forces imposed by the dilute flow overriding the dense flow and then roughly estimate Re as

$$\mathrm{Re} \approx \frac{\rho h \langle \bar{u} \rangle}{(\sigma_s / \dot{\gamma})} \approx \frac{\rho h \langle \bar{u} \rangle}{\rho g h \sin\theta / (\langle \bar{u} \rangle / h)} = \frac{\langle \bar{u} \rangle^2}{gh\sin\theta} = \frac{\mathrm{Fr}^2}{\tan\theta}, \quad (15)$$

where ρ is the bulk density of the flowing snow. Results of the depth averaging and estimated quantities are given in Table 1. Note that the estimates of Fr and Re implicitly assume constant flow density. The relatively short averaging intervals in which the flow was coherent and dense and where the velocities over all flow heights were more-or-less constant (at least did not change over orders of magnitude) allow us to assume a constant mean density over these short time intervals: we do not address the dilute flows but confine ourselves to time intervals in the dense steady-flow regime.

Plotting the mean shear rate, $\dot{\gamma}$, and the depth-averaged standard deviation, $\langle \delta u \rangle$, of the velocity as functions of the measured discharge, Q, we notice a general tendency for both to increase with increasing discharge (Fig. 11). From the plots we estimate $\dot{\gamma} \sim Q^\alpha$ with $\alpha \approx 1.7 \pm 0.1$ (Fig. 11a) and $\langle \delta u \rangle \sim Q^\beta$ with $\beta \approx 0.7 \pm 0.2$ (Fig. 11b). This indicates that the mean fluctuation magnitude is approximately proportional to the ratio of the mean shear rate and the discharge:

$$\langle \delta u \rangle \sim \dot{\gamma} Q^{\beta - \alpha} \approx a_1 \dot{\gamma}/Q + a_2, \qquad (16)$$

where a_1 and a_2 are constants. For these crude estimates, we performed (linear) least-squares fits on the log–log plots of the data, where the data points, y_i, were weighted by their uncertainties, δy_i, using instrumental weighting, $w_i \sim 1/(\delta y_i)^2$. Uncertainties of the scaling exponents are given in terms of the width of the 90% confidence intervals of the slope parameter of the linear fit.
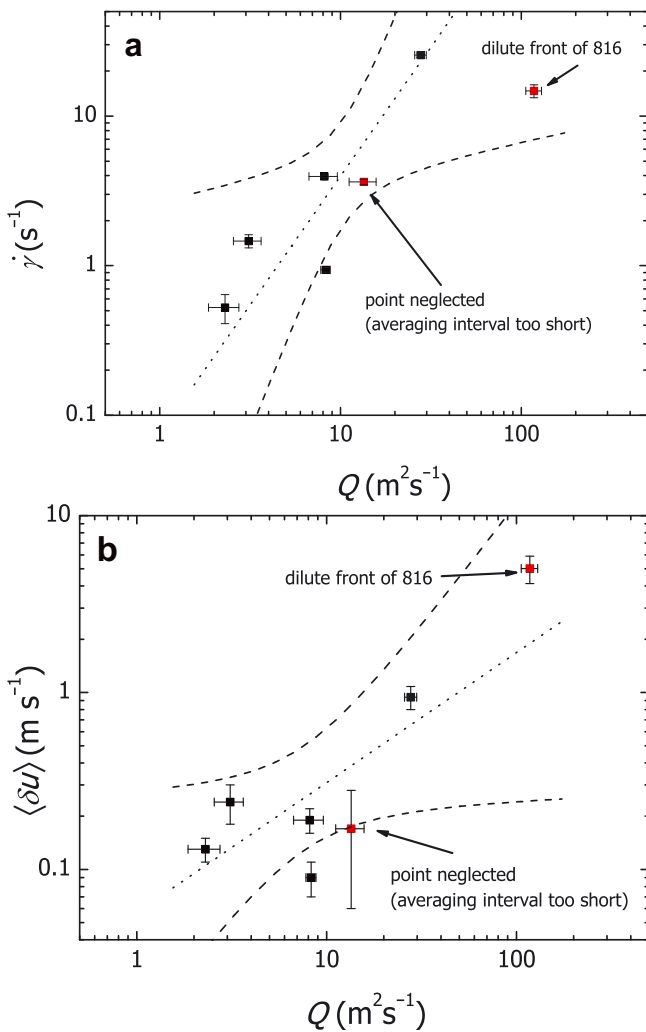
Fig. 11. (a) Mean shear rate, $\dot{\gamma}$, as a function of the discharge, Q. (b) Variation in velocity, $\langle \delta u \rangle$, as a function of discharge, Q. The results show that both the mean shear rate and variations in velocity increase with increasing discharge. Dotted curve: slope obtained by linear fit on log–log plot of the data; dashed curves: 90% confidence bands.

Fig. 12. Depth-averaged velocity variations as a function of the mean shear rate, $\dot{\gamma}$. Dotted curve: slope obtained by linear fit on log–log plot of the data; dashed curves: 90% confidence bands.

Figure 12 indicates an increase in the depth-averaged variation magnitude with the mean shear rate. Using the same estimating procedure as for the discharge dependencies, we can give a raw numerical estimate of this dependency: $\langle \delta u \rangle \sim \dot{\gamma}^{\alpha}$ with $\alpha = 0.5 \pm 0.1$.

These observations cover a broad variety of avalanche behaviour ranging from dry-fast to wet-dense flow behaviour at different stages of the flow (front, core and decelerating tail). We here report these relations as the first quantitative observations from real-scale avalanches and note that our experimental set-up is able to produce consistent results.

We now characterize the observed avalanches by their Froude numbers. The values listed in Table 1 show that Fr decreases from front to tail for avalanches No. 7226 and No. 816. For both avalanches, the front exhibits supercritical flow behaviour (Fr > 1). The subcritical behaviour of the tails (Fr < 1) indicates that there has been a transition from supercritical to subcritical flow in addition to the transition from shear to plug-flow behaviour. Note that the value of Fr = 1.4 ± 0.3 for the averaging interval of [32.4 s, 33.15 s] of avalanche No. 816 indicates a flow state close to the transition from super- to subcritical. Avalanche No. 8448 is
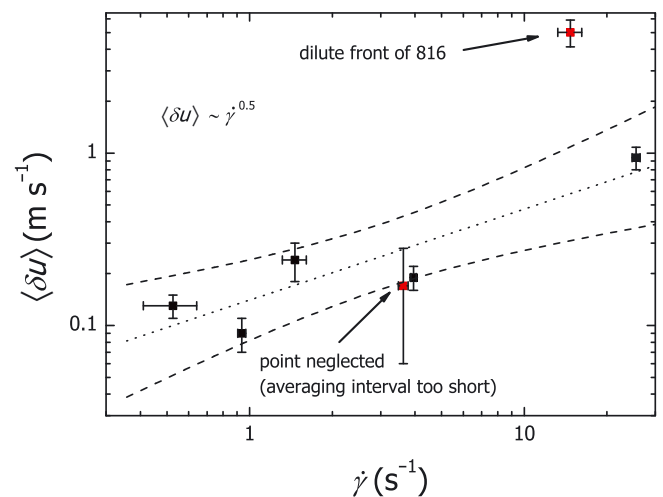
in the subcritical flow regime, exhibiting low shear except in the narrow basal shear layer. (Though the Froude number has been determined from the averaging interval [72 s, 74 s], comparison with Figure 7 makes clear that Fr should not vary significantly throughout the extended averaging interval [40 s, 80 s].) For the avalanches considered in this study, our observations indicate that shear flows tend to be supercritical and that the plug flows occur preferentially in subcritical flows.

The estimates for the Reynolds number in Table 1 give Re < 170 ≪ 2000, which suggests 'laminar' flow behaviour in the sense of the effective viscosity approach. Note that this estimate could be misleading if the flow rheology contains low-viscosity components that lead to much lower effective viscosity and, accordingly, to Reynolds numbers in the turbulent regime. The downslope component of gravity would then have to be balanced by Reynolds stresses of a highly turbulent flow. This could happen for Bingham-like rheologies where the threshold stress is related to weak snow cohesion and the shear stress above the threshold decreases with the shear rate (Kern and others, 2004). However, we judge this possibility to be unlikely for the avalanches under consideration. In the laminar regime, though, in all flows we observe significant velocity fluctuations that increase with the mean velocity. As for the discharge relations, we estimate the shape of the dependency by fitting the data in Figure 13 and find that $\langle \delta u \rangle$ is roughly proportional to $\langle \bar{u} \rangle^{2/3}$. In the range of errors, this is compatible with the dependency $\langle \delta u \rangle \sim \dot{\gamma} Q^{\beta - \alpha} \approx a_1 \dot{\gamma}/Q + a_2$, stated earlier.

We relate the generation mechanism of the velocity variations to the roughness of the sliding surface or to granular mechanical processes in the shear layer that generate particle-velocity fluctuations, rather than to viscous flow instabilities.

Our measurements provide evidence only for effects taking place on a timescale of 1–2 s. Nevertheless, we believe that our observations could be interpreted as a macro-scale representation of microscale processes that are not accessible with our present experimental set-up: results of numerical granular flow experiments indicate that macro-scale behaviour of particle-velocity fluctuations can be

related to the statistics of microscale fluctuations (Kern and others, 2005).

CONCLUSIONS

We have discussed the method of optical velocity measurements with special regard to possible sources of error on an elementary level and have outlined methods for improving the reliability of results.

Non-intrusive measurements of internal avalanche velocities (e.g. by nuclear magnetic resonance) are expensive, require huge technical effort and are practically unrealistic. For this reason, optical velocity measurements of the flow passing a flow-parallel wall are, at present, the best available method to measure real-scale avalanche velocity which is economically feasible with reasonable technical effort. When incoherent and spurious signals are removed from the measurements, the velocity data can provide useful information on the structure of the flow, even if the entire signal cannot be analysed.

The evolution of velocity profiles from the head to the tail of the avalanche could be obtained: the measured velocities vary strongly with the height above the ground, indicating the influence of the bottom boundary (running/sliding surface). At the front of the avalanche and for high velocities, the disturbance produced at the boundary is associated with significant shear throughout the flow depth. As this disturbance decays rather rapidly with distance from the bed at the tail (i.e. plug flow on a thin shear layer or a sliding surface), we suspect that the shear resistance or the internal strength of the flowing snow undergoes a change along the avalanche. This effect is most probably linked to a variable rheology and should be investigated further.

We determined the mean deviation of the velocities from the mean velocity at different flow heights, and found the magnitude of the deviations to increase with the mean velocities. The device errors are independent of the magnitude of the measured velocities. Consequently, these fluctuations cannot be due to the measurement equipment; rather they are an inherent property of the flow. We conclude that the magnitude of the fluctuations depends on the discharge of the flow or the flow velocity. We characterized the dense flows to be 'laminar' in the framework of the effective viscosity approach, the fast ones undergoing a transition from supercritical to subcritical from the head to the tail. The existence of velocity fluctuations in the laminar flow regime hints at a fluctuation-generating mechanism that is of a granular-mechanical rather than a continuum-mechanical nature.

Our observations on the evolution of the Froude number at different positions of the avalanche will have consequences for the design of avalanche braking and retarding structures such as mounds (Hákonardóttir and others, 2001, 2003) and dams (Baillifard, 2007; Baillifard and others, 2007): design procedures make extensive use of the decision whether the flow is sub- or supercritical. In this respect, we suggest that it is of enormous importance when designing avalanche-retarding structures to estimate the masses involved in the sub- and supercritical flow parts; it will be necessary to install additional capacitive density sensors (Louge and others, 1997) to obtain this information.

Other results are less conclusive. We cannot make a definite statement on whether an avalanche flows on a discrete sliding surface with a slip velocity, or whether a shear
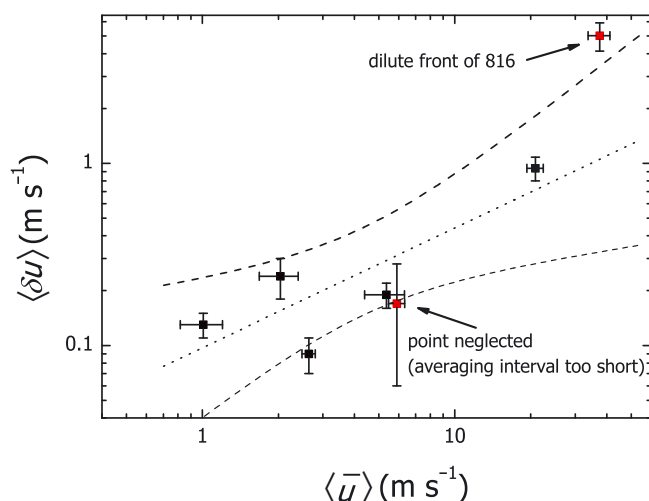

Fig. 13. Depth-averaged velocity variations, $\langle \delta u \rangle$, as a function of depth-averaged flow velocity, $\langle \bar{u} \rangle$.

layer exists at the bottom of the avalanche with some finite height. We could not resolve this question with the spatial resolution of the sensors. It is strongly recommended that the distance between sensors is reduced in order to address this and other problems.

ACKNOWLEDGEMENTS

REFERENCES

Baillifard, M.-A. 2007. Interaction between snow avalanches and catching dams. (PhD thesis, ETH Zürich.)

Baillifard, M.-A., M. Kern and S. Margreth. 2007. *Dimensionnement de digue d'ârret pour avalanches: demarche à suivre.* Davos, Swiss Federal Institute for Snow and Avalanche Research.

Bouchet, A., M. Naaim, F. Ousset, H. Bellot and D. Cauvard. 2003. Experimental determination of constitutive equations for dense and dry avalanches: presentation of the set-up and first results. *Surv. Geophys.*, **24**(5–6), 525–541.

Dent, J.D., K.J. Burrell, D.S. Schmidt, M.Y. Louge, E.E. Adams and T.G. Jazbutis. 1998. Density, velocity and friction measurements in a dry-snow avalanche. *Ann. Glaciol.*, **26**, 247–252.

Gauer, P., M. Kern, K. Kristensen, K. Lied, L. Rammer and H. Schreiber. 2007. On pulsed Doppler radar measurements of avalanches and their implication to avalanche dynamics. *Cold Reg. Sci. Technol.*, **50**(1–3), 55–71.

Gray, J.M.N.T., Y.-C. Tai and S. Noelle. 2003. Shock waves, dead zones and particle-free regions in rapid granular free-surface flows. *J. Fluid Mech.*, **491**, 161–181.

Gubler, H. 1987. Measurements and modelling of snow avalanche speeds. *IAHS Publ.* 162 (Symposium at Davos 1986 – *Avalanche Formation, Movement and Effects*), 405–420.

Hákonardóttir, K.M. and A.J. Hogg. 2005. Oblique shocks in rapid granular flows. *Phys. Fluids*, **17**(7), 077101. (10.1063/1.1950688.)

Hákonardóttir, K.M., T. Jóhannesson, F. Tiefenbacher and M. Kern. 2001. *A laboratory study of the retarding effect of breaking mounds in 3, 6 and 9 m long chutes*. Reykjavík, Veõurstofa Íslands. (Technical Report V01007.)

Hákonardóttir, K.M., A.J. Hogg, T. Jóhannesson, M. Kern and F. Tiefenbacher. 2003. Large-scale avalanche braking mound and catching dam experiments with snow: a study of the airborne jet. *Surv. Geophys.*, **24**(5–6), 543–554.

Issler, D., *ed*. 1999. European avalanche test sites. Overview and analysis in view of coordinated experiments. *Eidg. Inst. Schnee-Lawinenforsch. Mitt.* 59.

Issler, D. 2003. Experimental information on the dynamics of dry-snow avalanches. *In* Hutter, K. and N. Kirchner, *eds. Dynamic response of granular and porous materials under large and catastrophic deformations*. Berlin, Springer, 109–160.

Kern, M., F. Tiefenbacher and J. McElwaine. 2004. The rheology of snow in large chute flows. *Cold Reg. Sci. Technol.*, **39**(2–3), 181–192.

Kern, M., O. Buser, J. Peinke, M. Siefert and L. Vulliet. 2005. Stochastic analysis of single particle segregational dynamics. *Phys. Lett. A*, **336**(4–5), 428–433.

Lied, K., A. Moe, K. Kristensen and D. Issler. 2002. *Full scale avalanche test site and the effect of the catching dam*. Oslo, Norwegian Geotechnical Institute. (NGI Report 581200-35.)

Lied, K., A. Moe, K. Kristensen and D. Issler. 2004. Ryggfonn. Full scale avalanche test site and the effect of the catching dam. *In* Naaim, M. and F. Naaim-Bouvet, *eds. Proceedings of the International Seminar on Snow and Avalanche Test Sites, Grenoble, 22–23 November 2001*. Grenoble, Cemagref, 25–98.

Louge, M.Y., R. Steiner, S.C. Keast, R. Decker, J.D. Dent and M. Schneebeli. 1997. Application of capacitance instrumentation to the measurement of density and velocity of flowing snow. *Cold Reg. Sci. Technol.*, **25**(1), 47–63.

McElwaine, J.N. and F. Tiefenbacher. 2003. Calculating internal avalanche velocities from correlation with error analysis. *Surv. Geophys.*, **24**(5–6), 499–524.

McElwaine, J.N. and B. Turnbull. 2005. Air pressure data from the Vallée de la Sionne avalanches of 2004. *J. Geophys. Res.*, **110**(F3), F03010. (10.1029/2004JF000237.)

Nishimura, K., N. Maeno, F. Sandersen, K. Kristensen, H. Norem and K. Lied. 1993. Observations of the dynamic structure of snow avalanches. *Ann. Glaciol.*, **18**, 313–316.

Rammer, L. 2004. The measurements on powder snow avalanches at the tube bridge in BSCHLABS Avalanche on Feb 21st 2000. *In* Naaim, M. and F. Naaim-Bouvet, *eds. Proceedings of the International Seminar on Snow and Avalanche Test Sites, Grenoble, 22–23 November 2001*. Grenoble, Cemagref, 185–203.

Rammer, L., K. Kristensen, K. Lied, H. Schreiber and W.L. Randeu. 1998. Radar measurements of snow avalanche full scale experiment in Ryggfonn. *In* Hestnes, E., *ed. 25 Years of Snow Avalanche Research at NGI. Proceedings of the Anniversary Conference, 12–16 May 1998, Voss*, Norway. Oslo, Norwegian Geotechnical Institute, 215–219. (NGI Publication 203.)

Rammer, L., M.A. Kern, U. Gruber and F. Tiefenbacher. 2007. Comparison of avalanche-velocity measurements by means of pulsed Doppler radar, continuous wave radar and optical methods. *Cold Reg. Sci. Technol.*, **50**(1–3), 35–54.

Schaer, M. and D. Issler. 2001. Particle densities, velocities and size distributions in large avalanches from impact-sensor measurements. *Ann. Glaciol.*, **32**, 321–327.

Schaerer, P.A. and A.A. Salway. 1980. Seismic and impact-pressure monitoring of flowing avalanches. *J. Glaciol.*, **26**(94), 179–187.

Sovilla, B., P. Burlando and P. Bartelt. 2006. Field experiments and numerical modelling of mass entrainment in snow avalanches. *J. Geophys. Res.*, **111**(F3), F03007. (10.1029/2005JF000391.)

Sovilla, B., M. Schaer, M. Kern and P. Bartelt. 2008a. Impact pressures and flow regimes in dense snow avalanches observed at the Vallée de la Sionne test site. *J. Geophys. Res.*, **113**(F1), F01010. (10.1029/2006JF000688.)

Sovilla, B., M. Schaer and L. Rammer. 2008b. Measurements and analysis of full-scale avalanche impact pressure at the Vallée de la Sionne test site. *Cold Reg. Sci. Technol.*, **51**(2–3), 122–137.

Tiefenbacher, F. and M. Kern. 2004. Experimental devices to determine snow avalanche basal friction and velocity profiles. *Cold Reg. Sci. Technol.*, **38**(1), 17–30.